ORIGINAL PAPER

N-terminal myristoylation alters the calcium binding pathways in neuronal calcium sensor-1

Kousik Chandra · Venkatesh Ramakrishnan ·
Yogendra Sharma · K. V. R. Chary

Abstract Neuronal calcium sensor-1 (NCS-1) interacts with many membranes and cytosolic proteins, both in a Ca^{2+}-dependent and in a Ca_{2+}-independent manner, and its physiological role is governed by its N-terminal myristoylation. To understand the role of myristoylation in altering Ca^{2+} response and other basic biophysical properties, we have characterized the Ca^{2+} filling pathways in both myristoylated (myr) and non-myristoylated (non-myr) forms of NCS-1. We have observed that Ca^{2+} binds simultaneously to all three active EF-hands in non-myr NCS-1, whereas in the case of myr NCS-1, the process is sequential, where the second EF-hand is filled first, followed by the third and fourth EF-hands. In the case of myr NCS-1, the observed sequential Ca^{2+} binding process becomes more prominent in the presence of Mg^{2+}. Besides, the analysis of ^{15}N-relaxation data reveals that non-myr NCS-1 is more dynamic than myr NCS-1. The overall molecular tumbling correlation time increases by approximately 20% upon myristoylation. Comparing the apo forms of non-myr NCS-1 and myr NCS-1, we found the possibility of existence of some substates, which are structurally closer to the holo form of the protein. There are more such substates in the case of non-myr NCS-1 than in the case of the myr NCS-1, suggesting that the former accesses larger volumes of conformational substates compared with the latter. Further, the study reveals that the possibility of Ca^{2+} binding simultaneously to different parts of the protein is more favourable in non-myr NCS-1 than in myr NCS-1.

Keywords Neuronal calcium sensor-1 · Spectral density · Parallel/sequential filling · EFβ-scaffold model · Monod–Wyman–Changeux model

Abbreviations

BMRB	BioMagResBank
CaM	Calmodulin
CaBP	Ca^{2+}-binding protein
CPMG	Carr–Purcell–Meiboom–Gill
EF2	Second EF-hand of neuronal calcium sensor-1
EF3	Third EF-hand of neuronal calcium sensor-1
EF4	Fourth EF-hand of neuronal calcium sensor-1
HSQC	Heteronuclear single quantum correlation
ITC	Isothermal titration calorimetry
MWC	Monod–Wyman–Changeux
myr	Myristoylated
NCS	Neuronal calcium sensor
NOE	Nuclear Overhauser effect
non-myr	Non-myristoylated
VILIP	Visinin-like protein

K. Chandra · V. Ramakrishnan · K. V. R. Chary (✉)
Department of Chemical Sciences,
Tata Institute of Fundamental Research,
Homi Bhabha Road,
Mumbai 400005, India
e-mail: chary@tifr.res.in

Y. Sharma
Centre for Cellular and Molecular Biology (CCMB),
Uppal Road, Hyderabad 500007, India

Introduction

Changes in the cytosolic Ca^{2+} concentration trigger neurotransmitter release. Such changes are controlled by

stimuli of different kinds, such as depolarization of the membrane, extracellular signaling molecules and intracellular messengers. The cytoplasmic Ca^{2+} concentration varies from approximately 10^{-7} M in a resting cell to 10^{-5} M in an activated cell. Increase in Ca^{2+} concentration is controlled by the influx of extracellular Ca^{2+} or the release of Ca^{2+} from internal stores such as endoplasmic reticulum [1, 2]. The Ca^{2+} that flows into the cytoplasm during the activated state becomes bound to a wide variety of Ca^{2+}-binding proteins (CaBPs) which are actually responsible for various cellular functions mediated by interaction with target proteins. The most studied CaBP is calmodulin (CaM) [3], which is expressed in all cells and tissues of eukaryotic organisms. CaM controls synaptic-vesicle recruitment via activation of Ca^{2+}/CaM-dependent protein kinases I and II. Besides, CaM is involved in postsynaptic changes during synaptic plasticity [4–6], inactivation of voltage-gated Ca^{2+} channels [7–9] and activation of K^+ channels [10–12] in a Ca^{2+}-dependent manner. In spite of such diverse activity, nature surprisingly produces additional members of the family. These are neuronal-specific EF-hand CaBPs, called neuronal calcium censor (NCS) proteins. Frequenin from yeast is the most primitive member of this family. Most of the members of this family, such as recoverin [13, 14], visinin-like protein (VILIP)-1 [6, 15, 16], VILIP-3 and neurocalcin δ [17–19], hippocalcin [20], NCS-1 [21] and guanyl cyclase activating protein 2 [22, 23], are believed to play specific roles. This can be attributed to the presence of a conserved myristoylation motif. The myristoylation can be readily achieved for most of the members of this family, as they have been shown to be substrates for N-myristoyltransferase in *Escherichia coli*.

The N-terminal myristoylation has been well characterized in the case of recoverin [24]. This leads to the concept of what is known as a Ca^{2+}–myristoyl switch. During such a switch, Ca^{2+} binding to the protein leads to extrusion of the myristoyl group from the Ca^{2+}-free form, which has a compact structure with the myristoyl group buried within a hydrophobic pocket formed by the residues belonging to the cryptic first EF-hand of NCS-1 (EF1). Recoverin thus becomes available for membrane targeting as the myristoyl group can now be inserted into a lipid bilayer. As a consequence of this, recoverin translocates to the plasma membrane and thus binds to membranes in a Ca^{2+}-dependent manner [24, 25]. Other NCS proteins, such as hippocalcin [26, 27], neurocalcin δ [28], VILIP-1 [29] and VILIP-3 [30], possess this Ca^{2+}–myristoyl switch and remain membrane-associated at elevated Ca^{2+} concentration only. To make this Ca^{2+}–myristoyl switch functional, a large conformational change takes place upon Ca^{2+} binding [31]. Interestingly, the myristoylation consensus sequence at the N terminus (MGXXXS), CPXG

(residues 39–42) in EF1 and the two swivels Gly-42 and Gly-96 [24] are highly conserved in most of the members of the NCS family, which includes NCS-1. On the other hand, ten residues that clamp the myristoyl group in the apo form of recoverin (Trp31, Tyr32, Phe49, Ile52, Tyr53, Phe56, Phe57, Phe83, Leu90 and Trp104) [24] are also conserved in NCS-1. Despite these many striking similarities, NCS-1 behaves in a remarkably different way as it remains membrane-associated even with the resting Ca^{2+} concentration [27]. In this backdrop, we set out to understand the functional properties of NCS-1, which has one cryptic (EF1) and three functional (the second, third and fourth EF-hands of NCS-1; EF2, EF3 and EF4, respectively) EF-hand motifs, and the effect of myristoylation on it. In this endeavour, we first characterized the response of NCS-1 towards changes in Ca^{2+} concentration as it transforms from the apo to the holo state. This enabled us to identify the microscopic Ca^{2+} filling pathways in both myristoylated (myr) and non-myristoylated (non-myr) forms. Further, we measured the differences in the dynamics of both of these forms using ^{15}N-relaxation data. Earlier, we characterized the regulatory (Ca^{2+}-specific) and structural (Ca^{2+}- or Mg^{2+}-binding) EF-hand motifs of NCS-1 [32]. In this work, we have used the microscopic information about both the Ca^{2+} filling pathways and the protein dynamics of myr and non-myr forms together to deconvolute how the calcium response of the protein is affected by myristoylation at a microscopic level.

Materials and methods

Preparation of myr and non-myr NCS-1

Uniformly ^{15}N labelled myr NCS-1 was prepared as described earlier [33]. For the preparation of non-myr NCS-1, the same protocol was used except that the antibiotic added to the culture was ampicillin alone, as it contained no pBB131, which is kanamycin-resistant. Further no myristic acid and sodium myristate were added to the culture and the overexpression was induced with 1 mM isopropyl β-D-thiogalactopyranoside for 5–6 h. The purification protocol was similar to the one used for the purification of myr NCS-1.

NMR

The NMR data was collected at 25 °C with a Bruker Avance 800 MHz NMR spectrometer equipped with a pulsed field gradient unit and a triple-resonance cryoprobe, with an actively shielded z-gradient. NMR measurements for both myr and non-myr NCS-1 were performed with 1.0 mM uniformly $^{13}C/^{15}N$ labelled and uniformly $^{13}C,^{15}N$

doubly labeled protein samples (pH 7.4) in a mixed solvent of 90% H_2O and 10% ^2H_2O. The experiments with uniformly $^{15}N/^{13}C$ labeled NCS-1 in its two forms included sensitivity-enhanced 2D [^{15}N, ^1H] heteronuclear single quantum correlation(HSQC) using water flip-back for water suppression, 3D CBCANH [34], 3D CBCA(CO)NH [35], 3D HNCO [36], 3D HN(CA)CO [37, 38] and 3D HNHA [39]. The data transformation and processing were done using a PC equipped with Felix 2002 (Molecular Simulations) and the data were analysed using CARA [40]. Proton chemical shifts were calibrated with respect to 2,2-dimethyl-2-silapentane-5-sulfonate at 25 °C (0 ppm). ^{13}C and ^{15}N chemical shifts were calibrated indirectly [41].

Assignment of myr and non-myr NCS-1

We reported earlier the ^1H, ^{13}C and ^{15}N resonance assignments of myr NCS-1 in its Ca^{2+}-bound form using the suite of multidimensional NMR experiments mentioned in the previous section and the assignments thus obtained were deposited in BioMagResBank (BMRB) under accession number 6942 [33]. With the knowledge of the ^1H, ^{13}C and ^{15}N chemical shifts of myr NCS-1, we assigned the spectra of non-myr NCS-1 in its holo form by looking for the spectral signatures in the vicinity of the corresponding spectra of myr NCS-1. Thus, we could unambiguously assign almost all the ^1H, ^{13}C and ^{15}N spins and the assignments thus obtained were deposited in BMRB under accession number 16334.

Ca^{2+} titration of NCS-1

Ca^{2+}-titration experiments with the apo forms of non-myr and myr NCS-1 were carried out at 25 °C by adding small aliquots of $CaCl_2$ from a 80 mM stock solution to 550 µl of 0.8 mM uniformly ^{15}N-labelled protein, which was prepared in Chelex-treated buffer [50 mM tris(hydroxymethyl)aminomethane, 100 mM KCl, 1 mM dithiothreitol, pH 7.4] containing 10% ^2H_2O. NMR titration experiments were performed using a triple-channel Varian Inova 600 MHz NMR spectrometer operating at a ^1H frequency of 599.86 MHz, equipped with a pulsed field gradient unit and an actively shielded triple-resonance z-gradient probe. Initially, for each titration a 1-µl aliquot of the stock solution of $CaCl_2$ dissolved in the same buffer was added to the NMR tube containing the protein solution, mixed thoroughly and the tube was immediately transferred to the magnet for recording sensitivity-enhanced 2D [^{15}N, ^1H]-HSQC spectra with the ^1H carrier placed at the H_2O resonance (4.69 ppm) and with the ^{15}N carrier at 119 ppm. The final part of the titration was carried out in larger steps. For myr NCS-1 and non-myr NCS-1, a total of 31 and 15 titrations were carried out, respectively. The experimental

time for each HSQC was 40 min, each one having 128 × 2,048 complex points and spectral widths of 1,792 and 7,200 Hz, along the ω_1 and ω_2 dimensions, respectively. The spectra thus obtained were processed using Felix 2002 (Molecular Simulations). Integral volumes for the individual [^{15}N, ^1H] cross-peaks in the resultant spectra were measured using Felix 2002 and normalized volumes were plotted against the metal-to-protein ratio.

^{15}N-relaxation data collection and analysis

^{15}N-relaxation data were used to study the dynamics of both myr and non-myr NCS-1. R_1, R_2 and nuclear Overhauser effect (NOE) were obtained using a 2D [^{15}N, ^1H] correlation spectroscopy based inversion recovery experiment (for the measurement of individual T_1 values) [42], a Carr–Purcell–Meiboom–Gill (CPMG) sequence (for the measurement of individual T_2 values) [43], and a steady-state {^1H–^{15}N}-NOE experiment. In this endeavour, pulsed-field gradients were used for both coherence transfer pathway selection and sensitivity enhancement [43, 44]. Quadrature detection in the indirect dimension was achieved using the States–TPPI method [45]. The T_1 and T_2 data were recorded as 128 × 2,048 complex data points with 48 scans for each t_1 transient, with the spectral widths along both dimensions mentioned earlier. The recycle delay was set to 1.5 and 1 s for T_1 and T_2 measurements, respectively. Eleven T_1 experiments with different inversion recovery delays ranging from 100 to 1,500 ms were performed. Likewise, 11 T_2 experiments were performed with CPMG delays in the range from 10 to 190 ms. The {^1H–^{15}N}-NOE spectra were recorded with 128 × 2,048 complex matrices with 64 scans for each complex t_1 point, both with and without proton saturation during the relaxation delay. A 2.5-s period of proton saturation was used in the NOE experiment. The relaxation data thus obtained were analysed using reduced spectral density analysis [46].

Data processing

The data collected with the Varian 600 MHz NMR spectrometer was processed using Felix 2002 (Molecular Simulations). The 2D data were zero-filled to 1,024 and 4,096 complex points along t_1 and t_2, respectively, and apodized using either 60°- or 70°-shifted sine-squared bell window functions along both dimensions for resolution enhancement. The final size of each 2D spectrum was 4,096 (ω_2) × 1,024 (ω_1). The 3D spectral data collected with the Bruker 800 MHz spectrometer were processed using Topspin 2.0 and the resonance assignments were carried out using TATAPRO [47] and CARA [41]; all the assignments thus obtained were deposited in BMRB under accession number 16334.

Determination of ^{15}N-relaxation parameters

SPARKY [48] was used to measure the intensities of the individual backbone ^{15}N–^{1}H cross-peaks in both T_1 and T_2 data and to fit each peak intensity versus time plot, using the following exponentially decaying function:

$$I(t) = A \exp(-Rt) \tag{1}$$

where $I(t)$ is the intensity of the ^{15}N–^{1}H cross-peak at the delay time t (ms) in the experiments used for the measurement of T_1 and T_2.

The ^{1}H–^{15}N heteronuclear NOE was calculated using the following the equation:

$$NOE = I_{sat}/I_{eq} \tag{2}$$

where I_{sat} and I_{eq} are the intensities of the individual ^{15}N–^{1}H cross-peaks in the spectra measured with and without proton saturation, respectively.

Reduced spectral density mapping

The relaxation parameters R_1 and R_2 of the ^{15}N spin and the heteronuclear {^{1}H–^{15}N} NOEs provide information about various spectral densities, $J(0)$, $J(0.87\omega_H)$ and $J(\omega_N)$. Once we have the information about these densities, we can correlate $J(0)$ with $J(\omega_N)/J(0.87\omega_H)$ following the procedure proposed by Lefevre et al. [46]. The spectral density functions are derived using the following equations.

$$J(0) = \frac{3}{2(3d' + c')}\left[-\frac{1}{2}R_1 + R_2 - \frac{3}{5}R_{NOE}\right] \tag{3}$$

$$J(\omega_N) = \frac{1}{3d' + c'}\left[R_1 - \frac{7}{5}R_{NOE}\right] \tag{4}$$

$$J(\omega_H) = \frac{1}{5d'}R_1 \tag{5}$$

$$R_{NOE} = \left[((^{15}N - {}^1H)NOE - 1) * R_1 * \left(\frac{\gamma_N}{\gamma_H}\right)\right] \tag{6}$$

The constants c'(equal to c^2) and d'(equal to $d^2/4$) are approximately equal to 1.25×10^9 and 1.35×10^9 (rad/s)^2, respectively, at 14.1 T.

Following Lefevre et al., one can prove that in the low-frequency range, the spectral density functions can be described with a limited number of contributions which are very similar from one residue to the other and the $J(\omega_N, 0.87\omega_H)$ values are linearly correlated to the corresponding $J(0)$ values. The linear equation is as follows:

$$J(\omega_N, 0.87\omega_H) = \alpha_{N,H}J(0) + \beta_{N,H} \tag{7}$$

The α and β values thus obtained from the plot of $J(\omega_N, 0.87\omega_H)$ versus $J(0)$ can then be used to estimate τ_m, the overall molecular tumbling correlation time, using the following equation as described by Lefevre et al. [46]:

$$2\alpha\omega_{N,0.87H}^2\tau^3 + 5\beta\omega_{N,0.87H}^2\tau^2 + 2(\alpha - 1)\tau + 5\beta = 0. \tag{8}$$

Results and discussion

Response of myr and non-myr NCS-1 to an alternation in Ca^{2+} concentration

Residues chosen to map the microscopic Ca^{2+} binding pathways

NMR spectroscopy can provide information about the microscopic Ca^{2+} binding pathways in any given Ca^{2+}-binding protein. However, this demands site-specific monitoring of each Ca^{2+} binding site individually during the entire course of a Ca^{2+}-titration experiment. Current understanding of the mechanism of Ca^{2+} binding in CaBPs was first provided by the EFβ-scaffold model. According to this model, which is applicable to all EF-hand proteins, the Ca^{2+} binding mechanism and the following conformational change are controlled by a central structural element called the EFβ-scaffold [49]. This EFβ-scaffold determines the position of bound Ca^{2+}. During the initial stages of the Ca^{2+} binding process, the metal ion is first coordinated to the N-terminal part of the Ca^{2+}-binding loop (first and third residues in Scheme 1) and immobilized by the EFβ-scaffold (region highlighted in yellow) and thereafter the torsional flexibility of the EFβ-scaffold drives the reorientation of the C-terminal part of the Ca^{2+}-binding loop, to position the bidentate Glu (the 12th residue in Scheme 1) ligand to complete the process of Ca^{2+} coordination. Within the Ca^{2+}-binding loop, the residues at the second, fourth, sixth, eighth and tenth positions participate in the Ca^{2+} coordination and hence all of them can act as markers to follow the Ca^{2+} binding process. Most importantly, the highly homologous Gly residue at the sixth position (Gly78, Gly114 and Gly162) of the three functional Ca^{2+}-binding loops (Scheme 1) exhibits a characteristic downfield shift in the Ca^{2+}-bound

Scheme 1 The primary sequence of various Ca^{2+}-binding loops present in neuronal calcium sensor-1 (NCS-1). The inactive first EF-hand of NCS-1 (*EF1*) is shown in *black*. Residues that coordinate with Ca^{2+} are highlighted in *red*. Residues that form the EFβ-scaffold are highlighted in *yellow*. *EF2*, *EF3*, *EF4* second, third and fourth EF-hands of NCS-1, respectively

form (holo) of the protein as described elsewhere [32, 50]. Additionally, the hydrophobic residues at the eighth position (Ile80, Ile116 and Leu164) of the three active Ca^{2+}-binding loops also exhibit a characteristic downfield shift in the holo state of the protein as the amide proton of the respective residues at the eighth position is hydrogen-bonded to the equivalent residue of the paired EF-hand, a part of the short β-sheet connecting the two Ca^{2+}-binding loops [46], and is also attached to carbonyl oxygen atom (C'O) of the respective seventh residue, which is incidentally co-coordinating with the Ca^{2+} atom, resulting in an appreciable deshielding of the ^{15}N spin of the residue at the eighth position owing to the reduction in the electron density in its vicinity, as a result of polarization of the O(7)=C(7)–N amido group [50]. Thus, the corresponding ^{15}N–$^1H^N$ cross-peaks act as additional markers to follow the metal binding process.

Ca^{2+} binding to non-myr NCS-1 exhibits parallel filling

There are three canonical Ca^{2+} binding sites in NCS-1: (1) residues 61–96 (site II), (2) residues 97–144 (site III) and

(3) residues 145–190 (site IV). The cross-peak volumes of the residues at positions 6 and 8, belonging to these Ca^{2+}-binding loops (Scheme 1), were monitored to follow the Ca^{2+} binding process. The spectral signatures of the three Gly residues (Gly78, Gly114 and Gly162) surprisingly start appearing almost simultaneously around a metal-to-protein concentration ratio of 0.5:1 onwards. At a metal-to-protein concentration ratio of approximately 0.5:1, sites II, III and IV become filled to an extent of approximately 8, 2 and 9%, respectively, as shown in Fig. 1a, implying that the Ca^{2+} binds to EF2, EF3 and EF4 simultaneously. At a metal-to-protein concentration ratio of 1.5:1, the three sites (II, III and IV) become filled to an extent of approximately 76, 76 and 78%, respectively. The trend was similar when we monitored the residues at the eighth position of the corresponding loops as their spectral signatures also start gradually increasing from a metal-to-protein concentration ratio of 0.5 onwards (data not shown). This trend continues until the metal-to-protein concentration ratio reaches 2.5:1 and all the sites become saturated and no further increase in the peak volumes of any of the above-mentioned peaks is


Fig. 1 Calcium filling pathways in **a** non-myristoylated (non-myr) NCS-1 and **b** myristoylated (myr) NCS-1. Normalized peak intensity versus metal-to-protein concentration ratio for the sixth residue of EF2 (Gly78), EF3 (Gly114) and EF4 (Gly162) is shown for each form
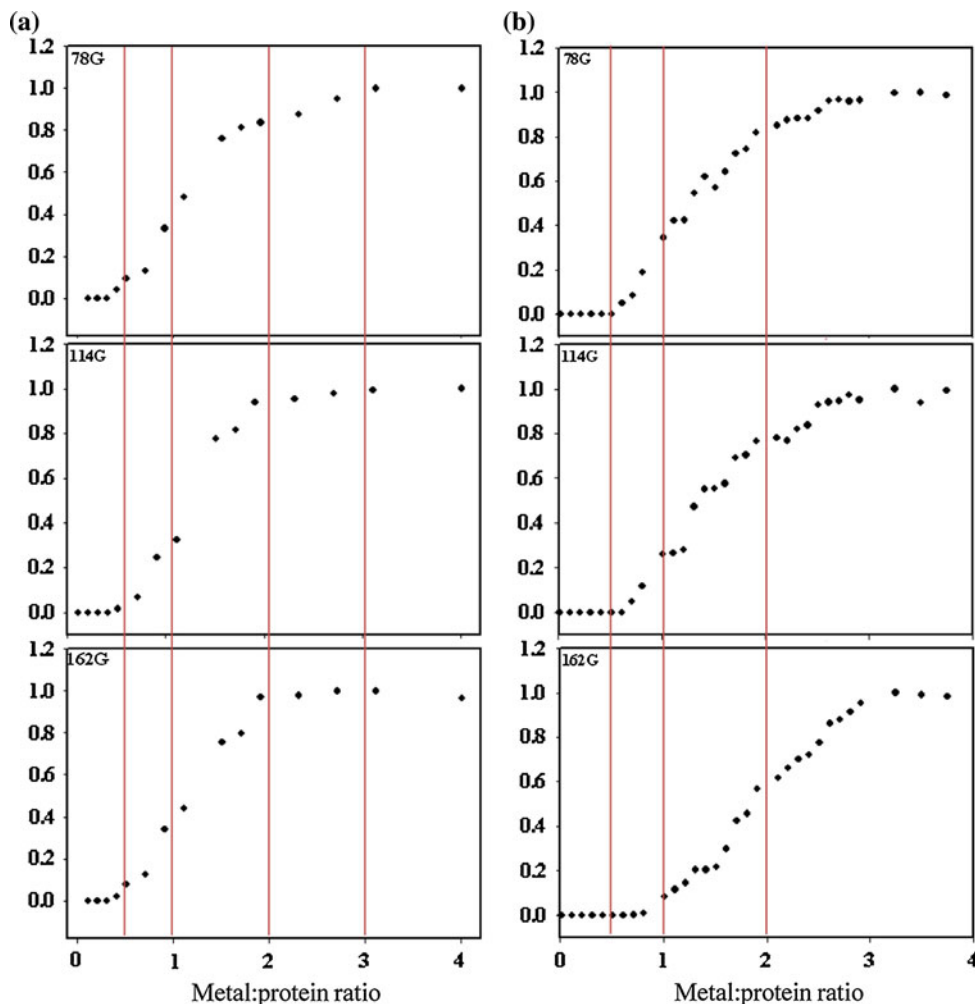
noticed. Thus, we conclude that the Ca^{2+} binding process in non-myr NCS-1 is indeed parallel as shown in Scheme 2a. This observation is in line with our previous results based on the isothermal titration calorimetry (ITC) data for this protein reported elsewhere [31]. Various species present in equilibrium observed during the course of the titration are denoted by 0, II, III and IV. The '0' represents the apo form of the protein and the roman numerals represent species where the metal binding site is occupied by the Ca^{2+}. For example, (II) represents the (Ca^{2+})(II)–NCS-1 species, where the second binding site alone is occupied by Ca^{2+}. Similarly (II, III) represents (Ca^{2+})(II)–(Ca^{2+})(III)–NCS-1, where both the second binding site and the third binding site are occupied by Ca^{2+}, and so on. There are eight possible species as non-myr NCS-1 exhibits parallel filling of all three sites during the course of titration as depicted in Scheme 2a.
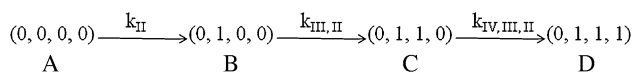
Ca^{2+} binding to myr NCS-1 exhibits sequentiality

During this set of Ca^{2+}-titration experiments with myr NCS1, the spectral signatures of the two Gly residues (Gly78 and Gly114) belonging to EF2 and EF3 start appearing together when the metal-to-protein concentration ratio is around 0.5:1, implying that EF2 and EF3 are almost being filled simultaneously with Ca^{2+}. Site IV starts being filled when the metal-to-protein concentration ratio is around 1.0:1, as shown in Fig. 1b. A careful examination of the spectral signatures of the above-mentioned residues, however, reveals that there is a clear sequentiality in the Ca^{2+} binding process, which is a thermodynamic process that depends on the conformation of the Ca^{2+}-binding loop, intrinsic affinity of individual binding site(s) and the extent of the conformational changes that take place upon Ca^{2+} binding. This sequential metal binding process could be established on the basis of the normalized intensity of Gly78 belonging to EF2, which is more than that of Gly 114 belonging to EF3. This trend was similar when we monitored the residues at the eighth position of the corresponding loops (data not shown). This is further ascertained by the observation that for all the recorded Ca^{2+}-titration points, the spectral signatures of site II have greater intensity than those of site III, whose spectral signatures in turn are greater compared than those of site IV. For example, at a metal-to-protein concentration ratio of 1:1, sites II, III and IV become filled to approximately 42, 27 and 12%, respectively. This trend continues until the metal-to-protein concentration ratio reaches 3:1, when all the sites become saturated. Thus, we conclude that the Ca^{2+} binding process in myr NCS-1 is indeed sequential (Scheme 2b). This observation is in line with our previous results based on the ITC data for this protein reported elsewhere [31]. As in
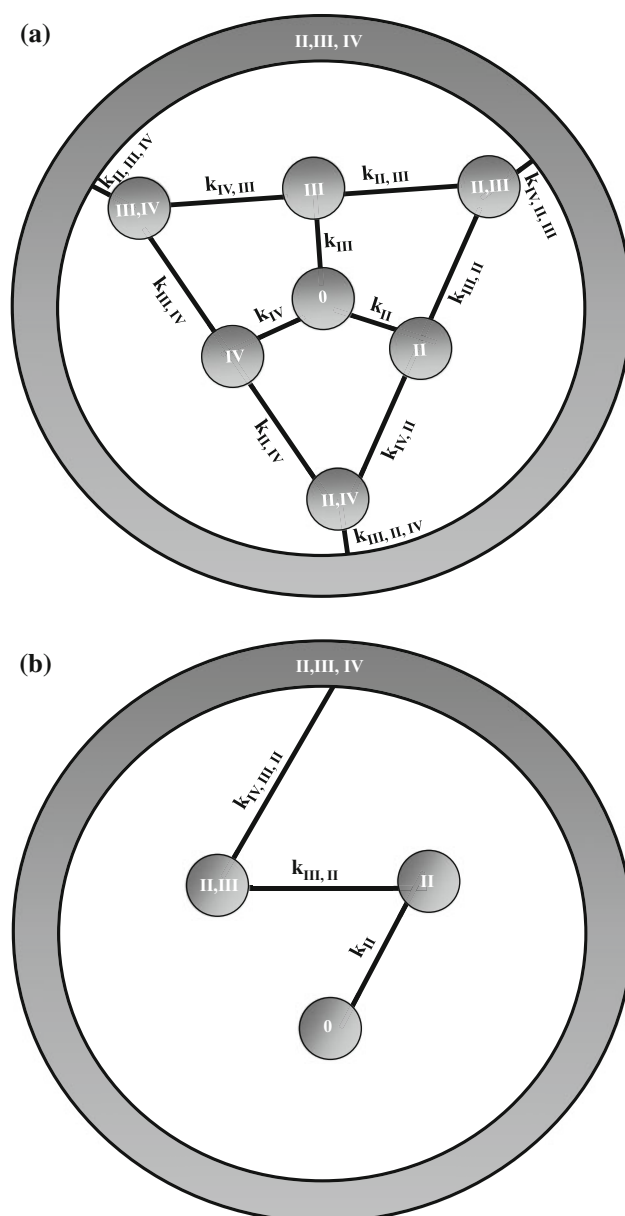
Scheme 2 a Calcium filling pathway of non-myr NCS-1, which exhibits parallel filling pathways. The '0' represents the apo form of the protein and the *roman numerals* represent species where the metal binding site is occupied by Ca^{2+}. *II* represents the (Ca^{2+})(II)-NCS-1 species, where the second binding site alone is occupied with Ca^{2+}. Similarly *II,III* represents (Ca^{2+})(II)–(Ca^{2+})(III)-NCS-1, where both the second binding site and the third binding site are occupied by Ca^{2+}, and so on. The associated binding constants are indicated. k_{II} is the microscopic binding constant of site II. $k_{III,II}$ is the microscopic binding constant of site III when site II is filled, and so on. **b** Calcium filling pathway of myr NCS-1, which exhibits sequential filling pathways. Ca^{2+} filling is initiated at site II, followed by site III and then at site IV. In the equilibrium, only four of the eight possible species are present. The associated binding constants are indicated

the case of non-myr NCS-1, various species present in equilibrium at different stages of the titration are denoted by 0, II, III and IV (Scheme 2b).

$$(0, 0, 0, 0) \xrightarrow{k_{II}} (0, 1, 0, 0) \xrightarrow{k_{III, II}} (0, 1, 1, 0) \xrightarrow{k_{IV,III,II}} (0, 1, 1, 1)$$
$$\quad A \qquad\qquad\quad B \qquad\qquad\quad C \qquad\qquad\quad D$$

Scheme 3 The Ca^{2+} binding process in the case of myr NCS-1. *0* and *1* represent absence and presence of Ca^{2+} in the respective binding loop. *A* is apo protein, *B* represents protein where Ca^{2+} is bound to site II, *C* represents protein where Ca^{2+} is bound to sites III and II and *D* represents protein where Ca^{2+} is bound to sites IV, III and II

We earlier studied the influence of Mg^{2+} on the Ca^{2+} binding process of myr NCS-1 by monitoring the changes in the spectral signatures of the Gly markers mentioned above during the course of yet another Ca^{2+}-titration experiment carried out with myr NCS-1, in the presence of Mg^{2+} [32]. We noticed the spectral signatures of Gly78 and Gly114 again appear one after another around a metal-to-protein concentration ratio of 0.5:1, similar to the observations made in the absence of Mg^{2+}. However, the spectral signatures of Gly162 belonging to the highly Ca^{2+} specific EF4 [32] started appearing only when the metal-to-protein concentration ratio reached approximately 1.7:1. Thus, the Ca^{2+} binding process shown in Scheme 3 becomes much more prominent in the presence of Mg^{2+}.

Determination of binding constants from NMR data

Experimental analysis of the binding energetics for an *n*-site system demands at least $2^n - 1$ (where *n* is the number of binding sites) independent observables. As a result, the site-specific analysis often becomes too complex even for low values of *n*. For non-myr NCS-1, there are 12 microscopic binding constants as depicted in Scheme 2a and to derive them at least seven independent observables are required. So for non-myr NCS-1, we could not derive the microscopic binding parameters from the NMR data alone. However, for myr NCS-1, we were able to fit the experimental data and derive the associated energetics, as it follows a simpler sequential model. In this case, since there are four possible species present in equilibrium at any given time, we need three microscopic binding constants to

describe the system. Thus, the Ca^{2+} binding process is simplified as depicted in Scheme 3.

In Scheme 3, k_{II}, $k_{III,II}$ and $k_{IV,III,II}$ represent intrinsic microscopic binding constants in the entire binding process. k_{II} represents the intrinsic microscopic binding constant of site II [in going from apo state A (0, 0, 0, 0) to state B, where Ca^{2+} is bound to the second site (0, 1, 0, 0)]. Likewise, $k_{III,II}$ and $k_{IV,III,II}$ represent intrinsic microscopic binding constants of site III when site II is filled, and that of site IV when sites II and III are filled, respectively.

We plotted the normalized intensities of the spectral signatures of the chosen Gly markers during the entire course of the reaction as a function of the metal-to-protein concentration ratio. These experimental plots were then fitted to determine the associated microscopic binding constants, k_{II}, $k_{III,II}$ and $k_{IV,III,II}$. The details of the procedure involved are given in the electronic supplementary material. The changes in the intensity of original Gly78 peak in the HSQC experiment were correlated to $(B + C + D)/C_0$ (where in C_0 is the total protein concentration, 0.0008 M, used in the present experiment), and the corresponding values of binding parameters thus obtained are provided in Table 1. It is worthwhile mentioning here that these microscopic binding parameters are of the same order as those measured earlier using ITC [31]. We also plotted the speciation graph of each species present in the equilibrium with the derived binding parameters (shown in the electronic supplementary material).

Dynamics of non-myrNCS-1 in the holo form

^{15}N-relaxation data were used to study the dynamics of non-myr NCS-1. The R_1, R_2 and NOE parameters were obtained for this protein by performing various experiments described in "Materials and methods". In spite of the large size of the protein, the HSQC shows a fair amount of dispersion in its spectral signatures as cross-peaks of 162 of 183 non-Pro residues were amenable for determining various relaxation parameters (Fig. 2). The first seven residues at the N-terminal end and Lys50 did not show their signatures in the HSQC owing to their involvement in

**Table 1** Thermodynamic parameters involved in Ca^{2+} filling pathways of myr NCS-1

Microscopic binding constants	Microscopic binding constants obtained from Gly78 data (M^{-1})[a]	Site loading energy $(kJ\ mol^{-1})$	Macroscopic binding constants	Macroscopic binding constants obtained from ITC (M^{-1})[b]	Site loading energy $(kJ\ mol^{-1})$
k_{II}	$(8.82 \pm 0.48) \times 10^4$	−28.21	K_1	$(1.67 \pm 0.06) \times 10^4$	−24.08
$k_{III,II}$	$(1.02 \pm 0.26) \times 10^7$	−40.15	K_2	$(1.89 \pm 0.09) \times 10^7$	−41.46
$k_{IV,III,II}$	$(1.68 \pm 0.45) \times 10^6$	−35.52	K_3	$(2.65 \pm 0.08) \times 10^6$	−36.62

ITC isothermal titration calorimetry

[a] These values are obtained using NMR data only

[b] These values are obtained from ITC measurements

Fig. 2 The residue-wise distribution of experimentally measured ^{15}N R_1, R_2 and nuclear Overhauser effect (NOE) data of non-myr NCS1 measured with a 800 MHz NMR spectrometer and the calculated spectral density functions [$J(0.87\omega_H)$, $J(\omega_N)$ and $J(0)$] along the sequence of amino acid residues. The secondary structural elements are shown in a sequence dependence manner in the top panel
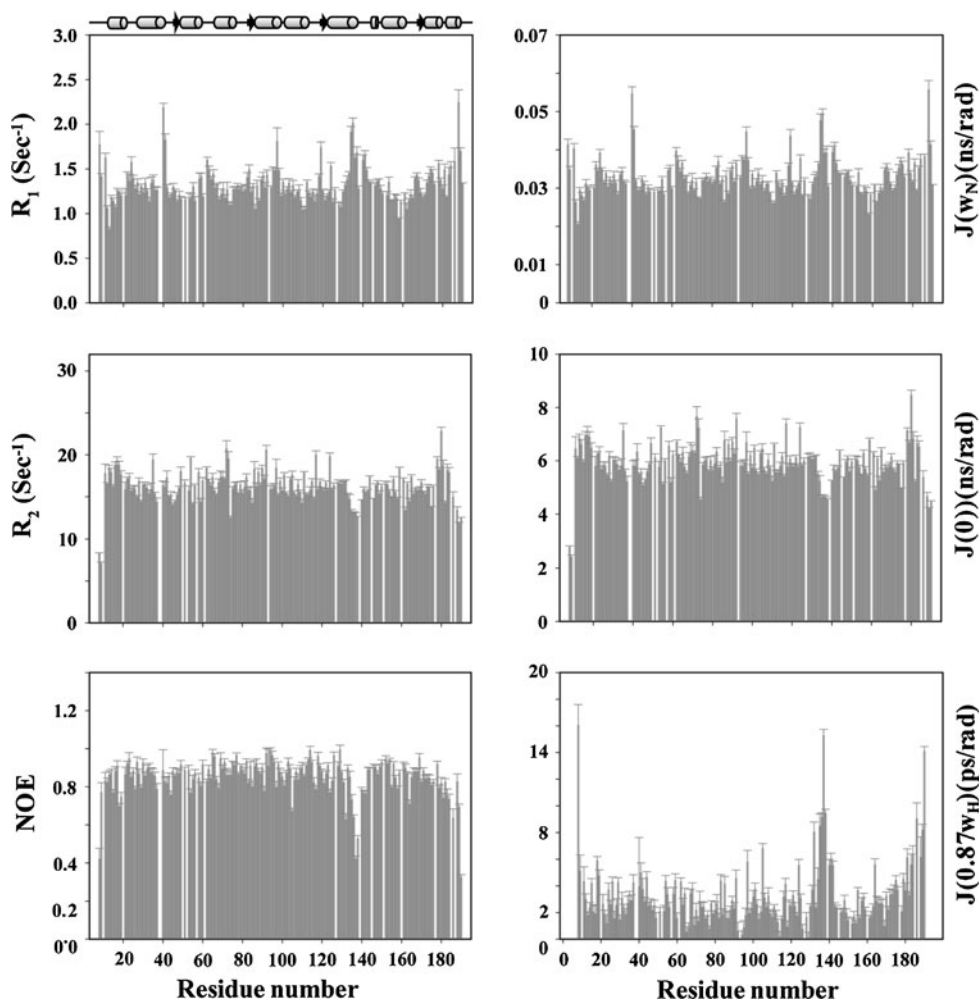
flexible regions. Some residues such as Ile35, Cys38, Thr66, Ser83, Ser93, Ile116 and Leu185 could not be considered for relaxation analysis owing to spectral overlap. The R_2 values for non-myr NCS-1 vary over a considerable range from 7.1 ± 0.6 to 22.8 ± 1.2 s^{-1}, with an average value around 16.1 ± 0.8 s^{-1}. Besides, the corresponding [^1H–^{15}N] steady-state NOE values cover a wide range from 0.32 to 0.99, with an average of 0.84, as expected for a structured protein. Overall, the distribution of the NOE values along the sequence is consistent with the R_2 values. The R_2 values of the residues in all ten α-helices present in the protein (Pro10-Lys19, Glu-24-Asp37, Ala45-Phe56, Thr62-Phe72, phe82-Arg94, Leu97-Tyr108, Arg118-Met131, Pro145-Met156, Leu166-Ala175 and Pro177-Leu183) vary within a small range from 15.8 ± 0.7 to 18.6 ± 0.8 s^{-1}, with an average value of 16.7 ± 0.9 s^{-1}. These α-helical stretches also show a higher average NOE, which can be attributed to their structural rigidity The residues (Lys9-Val12 and Tyr186-Val190) at the termini of both N- and C-terminal domains and loop regions (Gly59, Thr135-Glu138 and Leu97-Lys100) exhibit lower R_2 values owing to the greater flexibility. The

highly conserved Gly residues at the sixth position of the four EF-hand loops (Gly41, Gly78, Gly114 and Gly162) also show lower R_2 values (average 15.1). These Gly residues act as hinges during the metal binding process. The residues at the eighth position of the corresponding Ca^{2+}-binding loops (Leu43, Ile80, Ile116 and Ile164) also exhibit lower R_2 values (an average of 14.8), implying higher flexibility, which is crucial for the rotation around backbone bonds. Overall, the N-terminal domain of the protein shows higher average R_2 values (average 16.3 ± 1.2) compared with its C-terminal counterpart (average R_2 15.7 ± 1.1), implying greater motional flexibility in the C-terminal domain.

From the spectral density analysis it was observed that many residues such as Val13, Leu16, Thr17, Arg18, Ile35, Gln54, Thr62, Phe72, Asp73, Ile86, Ser90, Thr92, Leu97, Thr117, Ile124, Asn159, Ser178 and Val180 are found to have distinctly higher values of $J(0)$, indicating significant contributions of conformational exchange to the motion of corresponding NH vectors. This observation is consistent with the relaxation data for all these residues, which incidentally exhibit larger values of R_2. To probe this chemical
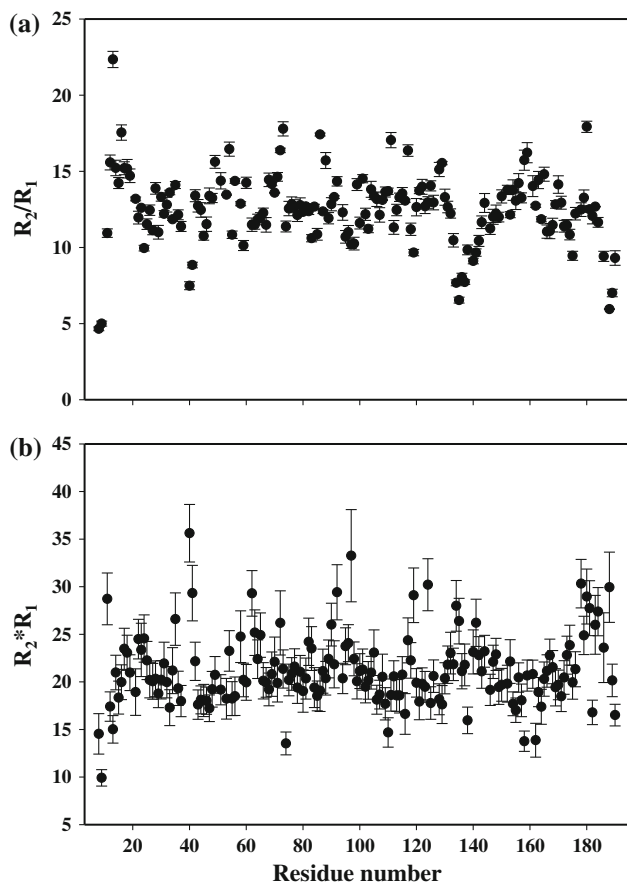
Fig. 3 *Top* The residue-wise distribution of ^{15}N R_1/R_2 of non-myr NCS1 measured with a 800 MHz NMR spectrometer used to probe the contribution from conformational exchange. *Bottom* The sequence-wise distribution of ^{15}N R_1R_2 of non-myr NCS1

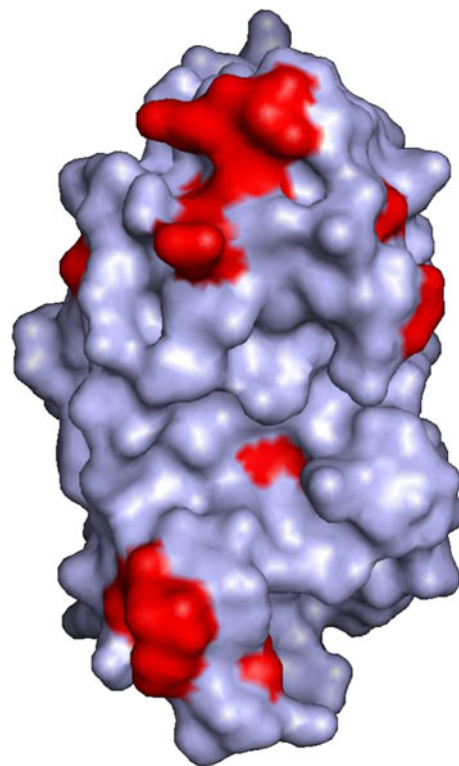

Fig. 4 Residues showing conformational exchange are mapped on the surface of non-myr NCS-1 and are highlighted in *red*. Most of these residues are solvent-exposed

exchange effect more efficiently, we monitored the sequence dependence of R_2/R_1 and R_2R_1 values, as depicted in Fig. 3, respectively. Most of the residues that showed higher R_2 values simultaneously show a higher R_2/R_1 ratio. For example, Val13, Leu16, Thr17, Gln54, Phe72, Asp73, Ile86, Thr117, Asn159 and Val180 show higher values of both R_2 and R_2/R_1. However, it is interesting that residues Val12, Glu14, Gln49, Ala88, Asp111, Ile128, Tyr129, Lys158, Asn159 and Thr165 are involved in a conformational exchange process although this was not obvious from their respective R_2 values alone. When we mapped the above-mentioned residues on the surface of the protein, we found that most of these residues are solvent-exposed as highlighted in red in Fig. 4. It is worth mentioning here that the crystal structure of non-myr NCS-1 shows a very large hydrophobic crevice with a dimensions as large as 30 Å × 31.5 Å × 31.5 Å, almost a quarter of its total size [51].

The correlation map of $J(\omega_N)$ versus $J(0)$ (Fig. 5) was used to derive τ_m for non-myr NCS-1. The three solutions thus obtained were 7.70 ns, 0.88 ns and −2.66 µs, with the most realistic value of τ_m being 7.70 ns. No realistic

solution could be derived on the basis of the linear dependence of $J(0.87\omega_H)$ versus $J(0)$.

Dynamics of myr NCS-1 in the holo form and comparison with non-myr NCS-1

Unlike in the case of non-myr NCS-1, the 2D [^{15}N, ^1H]-HSQC spectrum of myr NCS-1 shows moderate dispersion. Cross-peaks of 146 of 183 non-Pro residues were amenable for determining various relaxation parameters as depicted in Fig. 6. From ^1H, ^{13}C and ^{15}N resonance assignments [33], chemical shift indices were calculated using TALOS+ [52] to achieve secondary structural preferences as depicted in Fig. 6. The R_2 values for myr NCS-1 vary in a considerable range from 10.7 ± 0.8 to 24.7 ± 1.4 s^{-1}, with an average of 19.0 ± 1.5 s^{-1}, which is approximately 3.0 s^{-1} higher than for its non-myr counterpart. The polypeptide stretches which show α-helical propensities (Pro10-Arg18, Glu-24-Asp37, Ala45-Phe55, Thr62-Phe72, Phe82-Val91, Leu97-Tyr108, Arg118-Val132, Glu146-Met156, Leu166-Ala175 and Ser178-Ala182) have their R_2 values distributed within a small range of 18.8–21.1 s^{-1}, with an average value of 19.4 s^{-1}, reflecting the motional rigidity of these polypeptide stretches. The terminal residues of both N- and C-terminal domains show lower
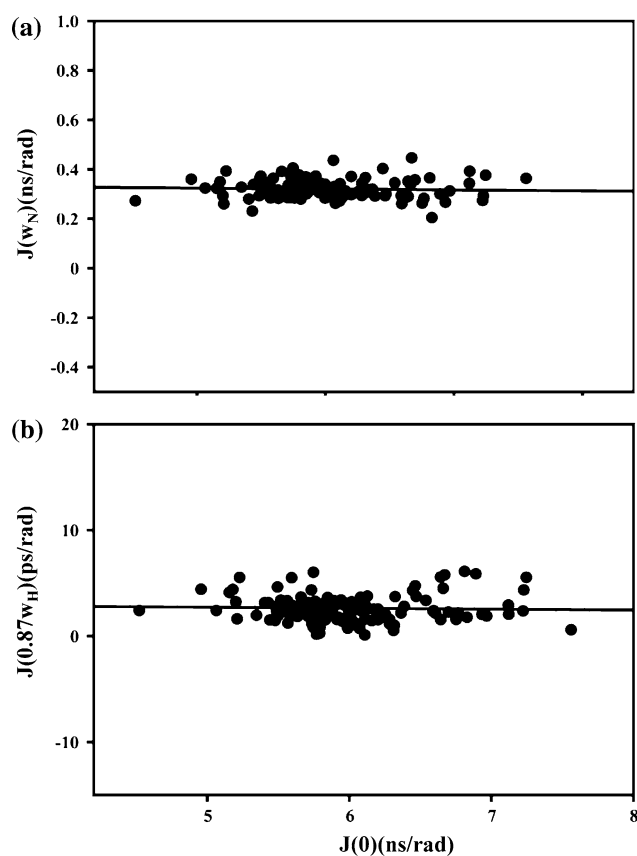
(a)

(b)

Fig. 5 *Top* The spectral density functions $J(\omega_N)$ versus $J(0)$ for non-myr NCS-1. *Bottom* The spectral density functions $J(0.87\omega_H)$ versus against $J(0)$ for non-myr NCS-1. The data were fitted with linear correlation between the spectral density functions: $J(\omega_N, 0.87\omega_H) = \alpha_{N,H} J(0) + \beta_{N,H}$

R_2 values owing to their greater flexibility. Residues that belong to the polypeptide stretches that show propensities of looplike structures also show lower R_2 values, which can again be attributed to higher motional flexibility. As in non-myr NCS-1, the residues at the sixth and eighth positions of the Ca^{2+}-binding loops show lower R_2 values. However, unlike non-myr NCS-1, the N-terminal domain of myr NCS-1 shows only a marginally higher average R_2 (average 19.1 ± 1.5) compared with the C-terminal counterpart (average R_2 18.8 ± 1.6), implying a nominal increase in motional flexibility in the C-terminal domain.

Spectral density analysis reveals that in myr NCS-1 some residues such as Thr17, Arg18, Gln54, Thr62, Asp73, Ile86, Thr92, Leu97, Thr117, Ile124, Asn159, Ser178, Val180, Gln181 and Leu183 have distinctly higher values of both $J(0)$ and R_2, indicating significant contributions to chemical exchange. To further confirm this sequence-wise distribution, R_2/R_1 and R_2R_1 were evaluated as shown in Fig. 7. The distribution of R_2/R_1 covers a large range from 11.24 ± 0.54 to 25.89 ± 0.86 over the entire amino acid sequence with an average of 18.93 ± 0.24. Most of the

above-mentioned residuessuch as Thr17, Arg18, Lys19, Phe22, Gln54, Asp73, Asn159, Val180, and Leu183 show higher R_2 values, as well as a higher R_2/R_1 ratio. On the other hand, residues Tyr21, Glu24, Trp30, Ile51, Glu74, Ala104, Asn112, Asp126, Lys158, Asn159 and Thr165, which show higher R_2/R_1 ratios do not show higher R_2 values, indicating the possibility of their involvement in exchange process with the solvent, and these residues may also be part of a possible hydrophobic crevice present in myr NCS-1, as in non-myr NCS-1.

The linear correlation seen between $J(\omega_N)$ and $J(0)$ (Fig. 8) was used to calculate the correlation time in the case of myr NCS-1, whereas the linear dependence of $J(0.87\omega_H)$ versus $J(0)$ (Fig. 8) could not provide a realistic value. The τ_m thus obtained for myr NCS-1 was found to be 9.11 ns, which is greater by 20% than that for non-myr NCS-1. This reveals the remarkable effect of myristoylation that reduces the dynamics of the protein to a large extent.

Factors affecting the Ca^{2+} binding process and role of dynamics to become a key deciding factor

The mechanism of the Ca^{2+} binding process is an interplay of many parameters that include the primary sequence of the protein, the structure in the protein in its apo state, the conformation of the Ca^{2+}-binding loop, the intrinsic affinity of individual binding site(s) and the extent of the conformational changes that take place upon Ca^{2+} binding. The conformational changes due to Ca^{2+} binding are controlled by the Ca^{2+} chelation of individual EF-hand loops. Initially, Ca^{2+} ion binds to the flexible N-terminal part of the loop, with the oxygen donors coming from the residues at positions 1, 3, 5 and 7 of the Ca^{2+}-binding loop. Then to accomplish the pentagonal bipyramidal geometry of Ca^{2+} coordination, the F-helix (the exiting helix) reorients itself to bring other residues of the C-terminal part, most importantly the residue at position 12 (Glu) of the loop, into the proper coordinating position. The movement of this helix is the main driving force for the observed conformational change in any EF-hand. Thus, the factors that assist this repositioning of the exiting helix play a major role in determining which EF-hand binds the Ca^{2+} first. Further, part of the Ca^{2+}-binding loop, namely 'the EFβ-scaffold', is responsible for the large diversity seen in EF-hand conformations. Residues at positions 7 and 8 of the individual Ca^{2+}-binding loops form the EFβ-scaffold and, interestingly, the backbone conformation of the eighth residue in the loop, with its permitted ranges of φ and ψ, generates a wide conformational space which encompass a large range of interhelical angles (the angle between the E and F helices [50]) that are observed in the different members of the subfamily of EF-hand proteins.

Fig. 6 The residue-wise distribution of experimentally measured ^{15}N T_1, T_2 and NOE data of myr NCS-1 measured with a 800 MHz NMR spectrometer and the calculated spectral density functions $[J(0.87\omega_H), J(\omega_N)$ and $J(0)]$ along the sequence of amino acid residues. The secondary structural propensities as obtained using TALOS+ are shown in the sequence dependence manner in the *top panel*
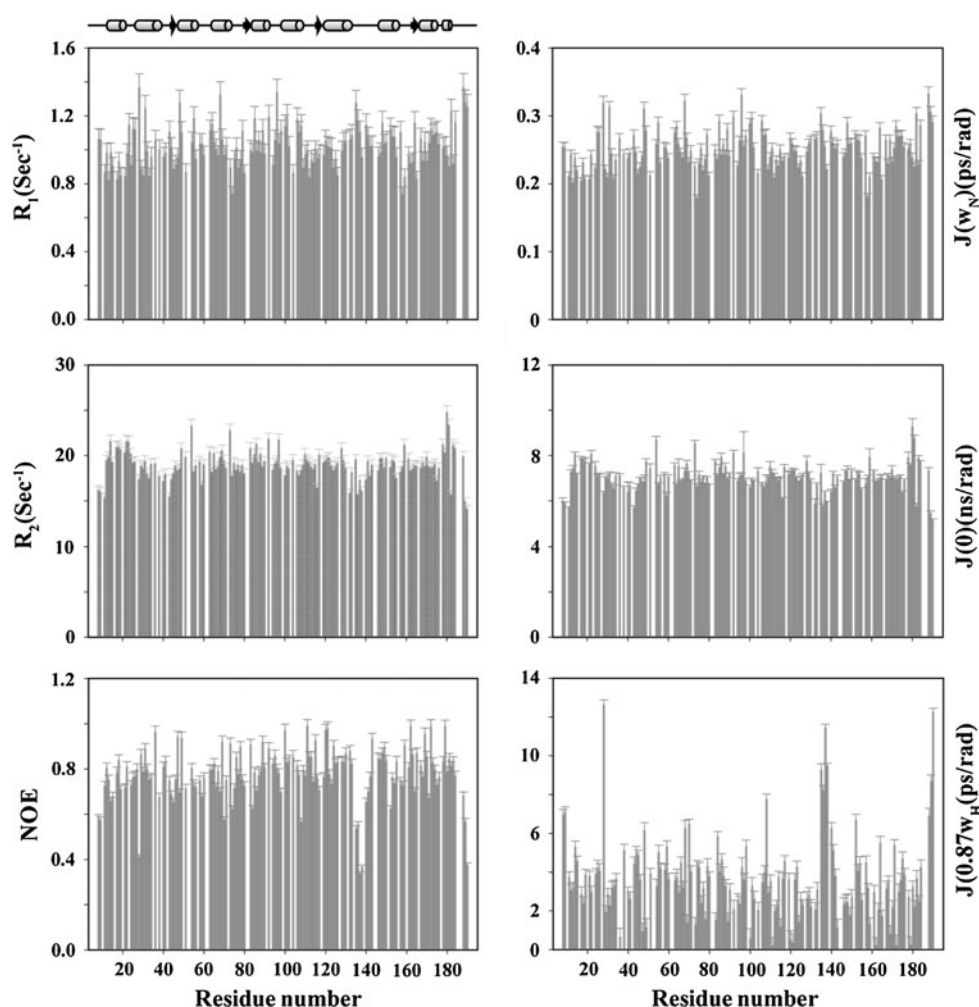
In this context, several attempts have been made to determine the minimum number of parameters required to describe the conformational space populated by most of the apo and holo EF-hand proteins [53]. However, to understand the details of the microscopic Ca^{2+} filling pathways exhibited by various EF-hands in a given protein, understanding the role of protein dynamics is very important. In fact, the members of the EF-hand superfamily were classified by studying the directions of the concerted interhelical movements of individual EF-hands [54, 55]. Molecular dynamics studies on various CaBPs [56–60] along with several experimental studies have also been used to correlate these kinds of concerted movements to the structural changes that generate a large conformational space [61–65]. The anisotropic and anharmonic disorder observed in the crystal structure of CaM [66] and the NMR relaxation data of both apo and holo CaM [66–69] suggest that CaM encompasses quasi-continuous substates, of which some partially interfere, throughout the Ca^{2+} binding process instead of just two well-defined conformations. This model is in complete agreement with the classical

Monod–Wyman–Changeux (MWC) model [70], which states that regulated proteins exist in different interconvertible states in the absence of any regulator and the regulators merely shift the equilibrium towards one state or another. In such a situation, it is the dynamics that control the sampling of substates. With an increase in the dynamics of the protein, access to more and more substates is possible as the conformational space increases with flexibility.

Though the dispersion in the backbone $^1H^N$ chemical shifts for the myr and non-myr NCS-1 in the apo form is 6.8–10.3 and 7.2–9.0 ppm, respectively, the corresponding $[^{15}N, ^1H]$-HSQC spectra (Fig. 9) show a fair degree of dispersion in the ^{15}N–$^1H^N$ peaks accounting for around 45 and 55% of all the expected peaks, respectively. Further, the spectra reveal that some peaks are broad and some of them are sharp. Such variable linewidths of peaks support the presence of several conformationally exchangeable species in the microsecond to millisecond timescale and their dynamic averaging [71, 72]. All these findings imply that the apo proteins adopt a molten-globule state in both forms; however, they are not identical in their apo state.
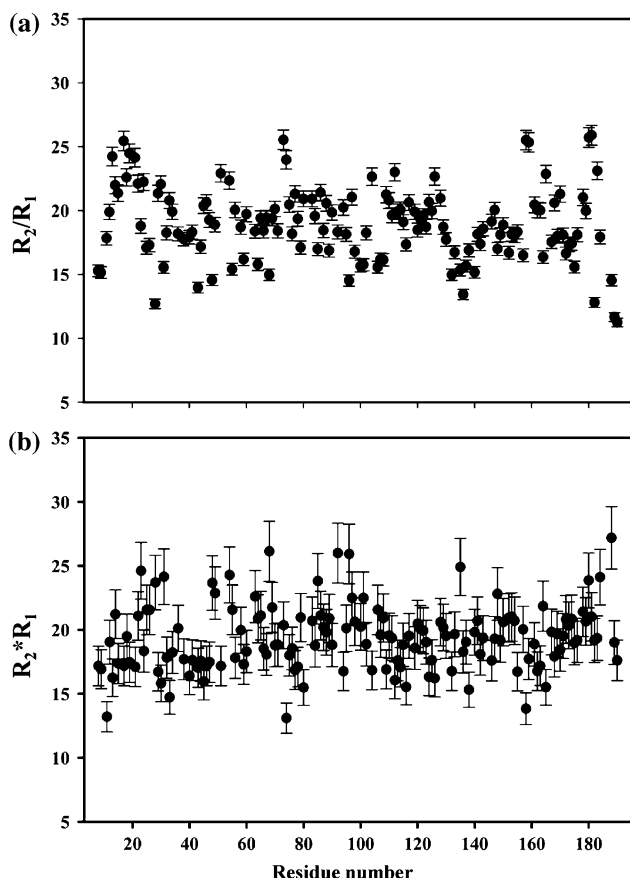
Fig. 7 *Top* The residue-wise distribution of ^{15}N R_1/R_2 of myr NCS-1 measured with a 800 MHz NMR spectrometer used to probe the contribution from conformational exchange. *Bottom* The sequence-wise distribution of ^{15}N R_1R_2 of non-myr NCS1

Fig. 8 The spectral density function for myr NCS-1. *Top* $J(\omega_N)$ versus $J(0)$. *Bottom* $J(0.87\omega_H)$ versus $J(0)$. The data were fitted with linear correlation between the spectral density functions: $J(\omega_N, 0.87\omega_H) = \alpha_{N,H} J(0) + \beta_{N,H}$

The non-myr NCS-1 in its apo form is relatively more structured than its myr counterpart in its apo form. The presence of a downfield-shifted peak at 10 ppm in the case of non-myr NCS-1 points to the presence of some substates which may be structurally closer to the holo form of the protein.

On the other hand, the backbone dynamics data of Ca^{2+}-bound forms of both non-myr and myr NCS-1 reveal that the former is much more dynamic than the latter. The data also reveal that the eighth residue of individual Ca^{2+}-binding loops in the holo form of non-myr NCS-1 possesses greater flexibility that will assist in their rotation around backbone bonds, which in turn results in sampling a large conformational space of the protein. Thus, non-myr NCS-1 may encompass a wider range of quasi-continuous substates because of its enhanced dynamics compared with myr NCS-1. The accessibility to larger volumes of conformational substates in turn increases the chance of the existencs of conformers that are intersecting in both the apo and the holo forms of the protein. On the basis of the MWC model described above, it can be stated that the possibility
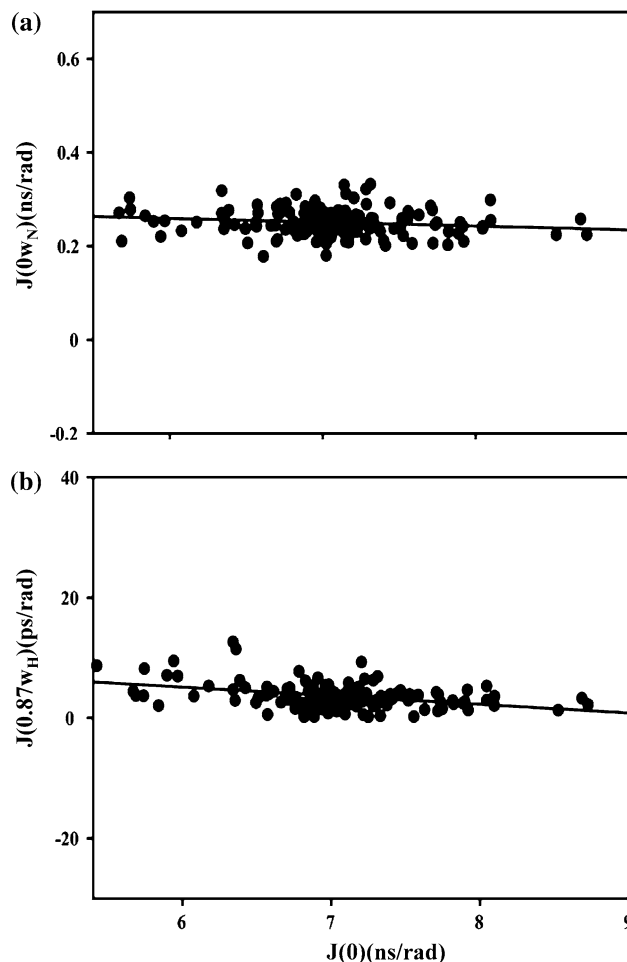
of Ca^{2+} binding simultaneously to the different parts of the protein is more favourable for the situation where final conformers are already present sparsely in some of the quasi-continuous substates which are present in the apo form of the protein. Once the metal binding to one of such conformers is initiated, the regulator (in this case Ca^{2+}) merely shifts the equilibrium towards the final structure (the holo form). Thus, the above description justifies the experimental observation of the parallel Ca^{2+} binding process in non-myr NCS-1 described above (Scheme 2a) compared with myr NCS-1, where the Ca^{2+} binding process is found to be sequential (Scheme 2b).

As described earlier by Aravind et al. [32.], the sequential microscopic Ca^{2+} binding process in the case of myr NCS-1 (Scheme 2b) becomes much more prominent in the presence of Mg^{2+}, during the transition from the Mg^{2+}-bound state to the holo state when compared with the transition from the Ca^{2+}-free (apo) state to the holo state. This can be explained as the consequence of Mg^{2+}

Fig. 9 The ^{15}N–^{1}H heteronuclear single quantum correlation of A non-myr NCS-1 and B myr NCS-1
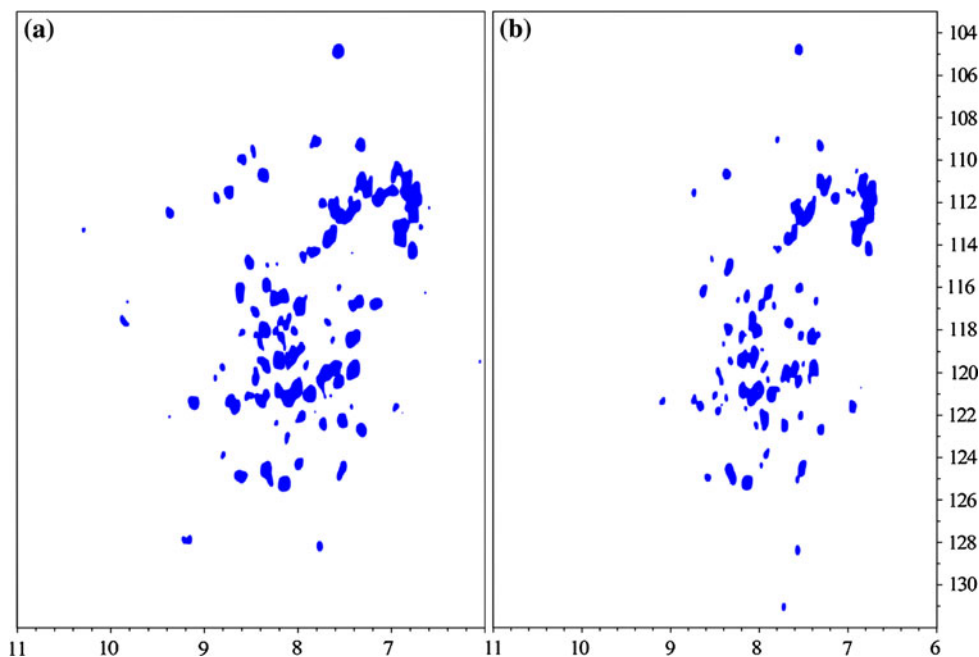
binding from a structural point of view. The Mg^{2+}-bound form of myr NCS-1 is found to be more structured than the apo form as the 2D [^{15}N, ^{1}H]-HSQC spectrum (data not shown) of Mg^{2+}-bound myr NCS-1 displays relatively sharper peaks (compared with those of apo myr NCS-1) and 66% of the peaks arise from the backbone amide region (21% more than for apo myr NCS-1). However, this is still less structured than the holo state. Hence, Mg^{2+}-bound myr NCS-1 is structurally closer to apo myr NCS-1. Mg^{2+} binds the same binding loop as Ca^{2+} does in an EF-hand. However, the extent of the conformational change in going from the Mg^{2+}-bound state to the Ca^{2+}-bound state is much less compared with that in going from the apo form to the Ca^{2+}-bound state. It is worth mentioning here that the Glu at position 12 of the Ca^{2+}-binding loop coordinates with Mg^{2+} in a monodentate manner instead of a bidentate fashion as is seen for Ca^{2+}. Further, the coordination of Mg^{2+} imparts a stringent requirement for octahedral coordination geometry and also a higher energetic cost of hydration owing to the smaller ionic radius. Thus, Mg^{2+} displacement by Ca^{2+} becomes much more amenable as the conformational cost is much lower. In the case of myr NCS-1, EF2 and EF3 have been identified as Ca^{2+}/Mg^{2+} sites or as structural sites, whereas EF4 is a Ca^{2+}-specific or regulatory site [32]. Thus, in the Mg^{2+}-bound state there exists a greater possibility of having some substates among the existing quasi-continuous substates that are close to the conformation that resembles a state partially filled (EF2 and EF3) by Ca^{2+}. This will initiate Ca^{2+} binding sequentially first to EF2 and then to EF3 (as observed experimentally). This will drive the equilibrium to partially filled (EF2 and EF3) conformers and will impart a delay in

initiating the filling of EF4. Thus, EF4, being a highly Ca^{2+} specific site, starts binding after the filling of EF2 and EF3, as conformational cost is greater.

Conclusion

We have successfully identified the Ca^{2+} binding processes in both non-myr and myr NCS-1. We observed that Ca^{2+} binds simultaneously to all the three active EF-hands in non-myr NCS-1, depicting a complete parallel filling. On the other hand, for myr NCS-1, the binding process is sequential (first to EF2, followed by EF3 and finally EF4). The observed sequential Ca^{2+} binding process becomes more prominent in the presence of Mg^{2+}. The analysis of ^{15}N-relaxation data revealed that non-myr NCS-1 is more dynamic than myr NCS-1. τ_m increases by 20% upon myristoylation. Comparing the apo forms of non-myr and myr NCS-1, we found the possibility of the existence of some substates, which are structurally closer to the holo form of the protein, is greater in the case of non-myr NCS-1. All these results suggest that non-myr NCS-1 accesses larger volumes of conformational substates. Following the MWC model [62], we can conclude that the possibility of Ca^{2+} binding simultaneously to the different parts of the protein is more favourable in non-myr NCS-1. Thus, this work demonstrates the relevance of myristoylation in the case of the response to an alteration in Ca^{2+} concentration and in terms of affecting the dynamics. This is of utmost importance as both of these properties are central to various functions of NCS-1 such as neurotransmitter release, exocytosis and interactions with other

known proteins, which are all controlled by an alteration of intracellular Ca^{2+} concentration.

References

1. Berridge MJ, Lipp P, Bootman MD (2000) The versatility and universality of calcium signalling. Nat Rev Mol Cell Biol 1:11–21
2. Berridge MJ, Bootman MD, Roderick HL (2003) Calcium signalling: dynamics, homeostasis and remodelling. Nat Rev Mol Cell Biol 4:517–529
3. Chin D, Means AR (2000) Calmodulin: a prototypical calcium sensor. Trends Cell Biol 10:322–328
4. Pettit DL, Perlman S, Malinow R (1994) Potentiated transmission and prevention of further LTP by increased CaMKII activity in postsynaptic hippocampal slice neurons. Science 266:1881–1885
5. Malinow R, Schulman H, Tsien RW (1989) Inhibition of postsynaptic PKC or CaMKII blocks induction but not expression of LTP. Science 245:862–866
6. Malenka RC, Kauer JA, Perkel DJ, Mauk MD, Kelly PT, Nicoll RA, Waxham MN (1989) An essential role for postsynaptic calmodulin and protein-kinase activity in long-term potentiation. Nature 340:554–557
7. Zuhlke RD, Pitt GS, Deisseroth K, Tsien RW, Reuter H (1999) Calmodulin supports both inactivation and facilitation of L-type calcium channels. Nature 399:159–162
8. Qin N, Olcese R, Bransby M, Lin T, Birnbaumer L (1999) Ca^{2+}-induced inhibition of the cardiac Ca^{2+} channel depends on calmodulin. Proc Natl Acad Sci USA 96:2435–2438
9. Lee A, Wong ST, Gallagher D, Li B, Storm DR, Scheuer T, Catterall WA (1999) Ca^{2+}/calmodulin binds to and modulates P/Q-type calcium channels. Nature 399:155–159
10. Fanger CM, Ghanshani S, Logsdon NJ, Rauer H, Kalman K, Zhou JM, Beckingham K, Chandy KG, Cahalan MD, Aiyar J (1999) Calmodulin mediates calcium-dependent activation of the intermediate conductance K–Ca channel, IKCa1. J Biol Chem 274:5746–5754
11. Keen JE, Khawaled R, Farrens DL, Neelands T, Rivard A, Bond CT, Janowsky A, Fakler B, Adelman JP, Maylie J (1999) Domains responsible for constitutive and Ca^{2+}-dependent interactions between calmodulin and small conductance Ca^{2+} activated potassium channels. J Neurosci 19:8830–8838
12. Xia XM, Fakler B, Rivard A, Wayman G, Johnson-Pais T, Keen JE, Ishii T, Hirschberg B, Bond CT, Lutsenko S, Maylie J, Adelman JP (1998) Mechanisms of calcium gating in small conductance calcium activated potassium channels. Nature 395:503–507
13. Dizhoor AM, Ericsson LH, Johnson RS, Kumar S, Olshevskaya E, Zozula S, Neubert TA, Stryer L, Hurley JB, Walsh KA (1992) The NH2 terminus of retinal recoverin is acylated by a small family of fatty acids. J Biol Chem 267:16033–16036
14. Zozulya S, Stryer L (1992) Calcium myristoyl protein switch. Proc Natl Acad Sci USA 89:11569–11573
15. Spilker C, Gundelfinger ED, Braunewell KH (1997) Calcium- and myristoyl-dependent subcellular localization of the neuronal calcium-binding protein VILIP in transfected PC12 cells. Neurosci Lett 225:126–128
16. Braunewell KH, Spilker C, Behnisch T, Gundelfinger ED (1997) The neuronal calcium-sensor protein VILIP modulates cyclic AMP accumulation in stably transfected C6 glioma cells: amino-terminal myristoylation determines functional activity. J Neurochem 68:2129–2139
17. Spilker C, Richter K, Smalla KH, Manahan-Vaughan D, Gundelfinger ED, Braunewell KH (2000) The neuronal EF-hand calcium-binding protein visinin-like protein-3 is expressed in cerebellar Purkinje cells and shows a calcium-dependent membrane association. Neuroscience 96:121–129
18. Faurobert E, Chen CK, Hurley JB, Teng DHF (1996) *Drosophila neurocalcin*, a fatty acylated, Ca^{2+}-binding protein that associates with membranes and inhibits in vitro phosphorylation of bovine rhodopsin. J Biol Chem 271:10256–10262
19. Ladant D (1995) Calcium and membrane-binding properties of bovine neurocalcin-delta expressed in *Escherichia coli*. J Biol Chem 270:3179–3185
20. Kobayashi M, Takamatsu K, Saitoh S, Noguchi T (1993) Myristoylation of hippocalcin is linked to its calcium-dependent membrane association properties. J Biol Chem 268:18898–18904
21. McFerran BW, Graham ME, Burgoyne RD (1998) Neuronal Ca^{2+} sensor 1, the mammalian homologue of frequenin, is expressed in chromaffin and PC12 cells and regulates neurosecretion from dense-core granules. J Biol Chem 273:22768–22772
22. Dizhoor AM, Hurley JB (1996) Inactivation of EF-hands makes GCAP-2 (p24) a constitutive activator of photoreceptor guanylyl cyclase by preventing a Ca^{2+}-induced "activator-to-inhibitor" transition. J Biol Chem 271:19346–19350
23. Oleshevskaya EV, Hughes EE, Hurley JB, Dizhoor AM (1997) Calcium binding, but not calcium–myristoyl switch, controls the ability of guanyl cyclase-activating protein GCAP-2 to regulate photoreceptor guanyl cyclase. J. Biol Chem 272:14327–14333
24. Ames JB, Ishima R, Tanaka T, Gordon JI, Stryer L, Ikura M (1997) Molecular mechanics of calcium–myristoyl switches. Nature 389:198–202
25. Tanaka T, Ames JB, Harvey TS, Stryer L, Ikura M (1995) Sequestration of the membrane-targeting myristoyl group of recoverin in the calcium-free state. Nature 376:444–447
26. O'Callaghan DW, Tepikin AV, Burgoyne RD (2003) Dynamics and calcium sensitivity of the Ca^{2+}/myristoyl switch protein hippocalcin in living cells. J Cell Biol 163:715–721
27. O'Callaghan DW, Ivings L, Weiss JL, Ashby MC, Tepikin AV, Burgoyne RD (2002) Differential use of myristoyl groups on neuronal calcium sensor proteins as a determinant of spatiotemporal aspects of Ca^{2+} signal transduction. J Biol Chem 277:14227–14237
28. Ivings L, Pennington SR, Jenkins R, Weiss JL, Burgoyne RD (2002) Identification of Ca^{2+}-dependent binding partners for the neuronal calcium sensor protein neurocalcin delta: interaction with actin, clathrin and tubulin. Biochem J 363:599–608
29. Spilker C, Dresbach T, Braunewell KH (2002) Reversible translocation and activity-dependent localization of the calcium–myristoyl switch protein VILIP-1 to different membrane compartments in living hippocampal neurons. J Neurosci 22:7331–7339
30. Spilker C, Braunewell KH (2003) Calcium–myristoyl switch, subcellular localization, and calciumdependent translocation of the neuronal calcium sensor protein VILIP-3, and comparison with VILIP-1 in hippocampal neurons. Mol Cell Neurosci 24:766–778
31. Jeromin A, Muralidhar D, Parameswaran MN, Roder J, Fairwell T, Scarlata S, Dowal L, Mustafi SM, Chary KVR, Sharma Y (2004) N-terminal myristoylation regulates calcium-induced conformational changes in neuronal calcium sensor. J Biol Chem 279:27158–27167
32. Aravind P, Chandra K, Reddy PP, Jeromin A, Chary KVR, Sharma Y (2008) Regulatory and structural EF-hand motifs of

neuronal calcium sensor-1: Mg^{2+} modulates Ca^{2+} binding, Ca^{2+}-induced conformational changes, and equilibrium unfolding transitions. J Mol Biol 376:1100–1115

33. Mukherjee S, Muralidhar D, Atreya HS, Szyperski T, Jeromin A, Sharma Y, Chary KVR (2006) ^1H, ^{13}C, and ^{15}N chemical shift assignments of neuronal calcium sensor-1, a multi-functional calcium-binding protein. J Biomol NMR 36:48

34. Wittekind M, Mueller L (1993) HNCACB, a high-sensitivity 3D NMR experiment to correlate amide-proton and nitrogen resonances with the alpha-carbon and beta-carbon resonances in proteins. J Magn Reson B 101:201–205

35. Grzesiek S, Bax A (1992) Correlating backbone amide and side-chain resonances in larger proteins by multiple relayed triple resonance NMR. J Am Chem Soc 114:6291–6293

36. Kay LE, Ikura M, Tschudin R, Bax A (1990) 3-Dimensional triple-resonance NMR-spectroscopy of isotopically enriched proteins. J Magn Reson 89:496–514

37. Clubb RT, Thanabal V, Wagner G (1992) A new 3D HN(CA)HA experiment for obtaining fingerprint H^N–H^α cross peaks in N^{15}-labeled and C^{13}-labeled proteins. J Biomol NMR 2:203–210

38. Clubb RT, Thanabal V, Wagner G (1992) A constant-time 3-dimensional triple-resonance pulse scheme to correlate intraresidue $1H^{(N)}$, N15, and $C'13$ chemical-shifts in N15–C13-labeled proteins. J Magn Reson 97:213–217

39. Vuister GW, Bax A (1993) Quantitative J correlation—a new approach for measuring homonuclear 3-bond $J(H^N$–$H^\alpha)$ coupling-constants in N^{15}-enriched proteins. J Am Chem Soc 115:7772–7777

40. Keller R (2004) The computer aided resonance assignment tutorial, 1st edn. CANTINA

41. Wishart DS, Bigam CG, Yao J, Abildgaard F, Dyson HJ, Oldfield E, Markley JL, Sykes BD (1995) ^1H, ^{13}C and ^{15}N chemical shift referencing in biomolecular NMR. J Biomol NMR 6:135–140

42. Vold RL, Waugh JS, Klein MP, Phelps DE (1968) Measurement of spin relaxation in complex systems. J Chem Phys 48:483831–483832

43. Cavanagh J, Palmer AG, Wright PE, Rance M (1991) Sensitivity improvement in proton-detected 2-dimensional heteronuclear relay spectroscopy. J Magn Reson 91:429–436

44. Palmer AG, Cavanagh J, Wright PE, Rance M (1991) Sensitivity improvement in proton-detected 2-dimensional heteronuclear correlation NMR-spectroscopy. J Magn Reson 93:151–170

45. Marion D, Ikura M, Tschudin R, Bax A (1989) Rapid recording of 2D NMR-spectra without phase cycling—application to the study of hydrogen-exchange in proteins. J Magn Reson 85:393–399

46. Lefevre JF, Dayie KT, Peng JW, Wagner G (1996) Internal mobility in the partially folded DNA binding and dimerization domains of GAL4: NMR analysis of the N–H spectral density functions. Biochemistry 35:2674–2686

47. Atreya HS, Chary KVR, Govil G (2002) Automated NMR assignments of proteins for high throughput structure determination: TATAPRO II. Curr Sci 83:1372–1376

48. Goddard TD, Kneller DG SPARKY 3. University of California, San Francisco, http://www.cgl.ucsf.edu/home/sparky/

49. Grabarek Z (2006) Structural basis for diversity of the EF-hand calcium-binding proteins. J Mol Biol 359:509–525

50. Malmendal A, Evenas J, Thulin E, Gippert GP, Drakenberg T, Forsen S (1998) When size is important accommodation of magnesium in a calcium binding regulatory domain. J Biol Chem 273:28994–29000

51. Bourne Y, Dannenberg J, Pollmann V, Marchot P, Pongs O (2001) Immunocytochemical localization and crystal structure of human frequenin (neuronal calcium sensor 1). J Biol Chem 276:11949–11955

52. Shen Y, Delaglio F, Cornilescu G, Bax A (2009) TALOS+: a hybrid method for predicting protein backbone torsion angles from NMR chemical shifts. J Biomol NMR 44:213–223

53. Babini E, Bertini I, Capozzi F, Luchinat C, Quattrone A, Turano M (2005) Principal component analysis of the conformational freedom within the EF-hand superfamily. J Proteome Res 6:1961–1971

54. Capozzi F, Luchinat C, Micheletti C, Pontiggia F (2007) Essential dynamics of helices provide a functional classification of EF-hand proteins. J Proteome Res 11:4245–4255

55. Capozzi F, Casadei F, Luchinat C (2006) EF-hand protein dynamics and evolution of calcium signal transduction: an NMR view. J Biol Inorg Chem 8:949–962

56. Micheletti C, Carloni P, Maritan A (2004) Accurate and efficient description of protein vibrational dynamics: comparing molecular dynamics and Gaussian models. Proteins 55(3):635–645

57. Bahar I, Erman B, Haliloglu T, Jernigan RL (1997) Efficient characterization of collective motions and interresidue correlations in proteins by low-resolution simulations. Biochemistry 36(44):13512–13523

58. Piana S, Carloni P, Parrinello M (2002) Role of conformational fluctuations in the enzymatic reaction of HIV-1 protease. J Mol Biol 319(2):567–583

59. Cascella M, Micheletti C, Rothlisberger U, Carloni P (2005) Evolutionarily conserved functional mechanics across pepsin-like, retroviral aspartic proteases. J Am Chem Soc 127(11):3734–3742

60. De Los Rios P, Cecconi F, Pretre A, Dietler G, Michielin O, Piazza F, Juanico B (2005) Functional dynamics of PDZ binding domains: a normal-mode analysis. J Biophys 89(1):14–21

61. Falke JJ (2002) Enzymology. A moving story. Science 295(5559):1480–1481

62. Rod TH, Radkiewicz JL, Brooks CL III (2003) Correlated motion, the effect of distal mutations in dihydrofolate reductase. Proc Natl Acad Sci USA 100(12):6980–6985

63. Delarue M, Sanejouand YH (2002) Simplified normal mode analysis of conformational transitions in DNA-dependent polymerases: the elastic network model. J Mol Biol 320(5):1011–1024

64. Alexandrov V, Lehnert U, Echols N, Milburn D, Engelman D, Gerstein M (2005) Normal modes for predicting protein motions: a comprehensive database assessment and associated Web tool. Protein Sci 14(3):633–643

65. Smith GR, Sternberg MJ, Bates PA (2005) The relationship between the flexibility of proteins, their conformational states on forming protein–protein complexes with an application to protein–protein docking. J Mol Biol 347(5):1077–1101

66. Wilson MA, Brunger AT (2000) The 1.0 angstrom crystal structure of Ca^{2+}-bound calmodulin: an analysis of disorder and implications for functionally relevant plasticity. J Mol Biol 301:1237–1256

67. Chou JJ, Li SP, Klee CB, Bax A (2001) Solution structure of Ca^{2+}-calmodulin reveals flexible hand-like properties of its domains. Nat Struct Biol 8:990–997

68. Zhang M, Tanaka T, Ikura M (1995) Calcium-induced conformational transition revealed by the solution structure of apo calmodulin. Nat Struct Biol 2:758–767

69. Tjandra N, Kuboniwa H, Ren H, Bax A (1995) Rotational-dynamics of calcium-free calmodulin studied by N15-NMR relaxation measurements. Eur J Biochem 230:1014–1024

70. Monod J, Wyman J, Changeux J-P (1965) On the nature of allosteric transitions: a plausible model. J Mol Biol 12:88–118

71. Schulman BA, Kim PS, Dobson CM, Redfield C (1997) A residue-specific NMR view of the non-cooperative unfolding of a molten globule. Nat Struct Biol 4:630–634

72. Baum J, Dobson CM, Evans PA, Hanley C (1989) Characterization of a partly folded protein by NMR methods—studies on the molten globule state of guinea-pig alpha-lactalbumin. Biochemistry 28:7–13